

## Revisiting argon cluster formation in a planar gas jet for high-intensity laser matter interaction

Y. Tao, R. Hagmeijer, E. T. A. van der Weide, H. M. J. Bastiaens, and K.-J. Boller

Citation: [Journal of Applied Physics](#) **119**, 164901 (2016); doi: 10.1063/1.4947187

View online: <http://dx.doi.org/10.1063/1.4947187>

View Table of Contents: <http://scitation.aip.org/content/aip/journal/jap/119/16?ver=pdfcov>

Published by the [AIP Publishing](#)

---

### Articles you may be interested in

[Production of neutrons up to 18 MeV in high-intensity, short-pulse laser matter interactions](#)

*Phys. Plasmas* **18**, 100703 (2011); 10.1063/1.3654040

[Formation of laser plasma channels in a stationary gas](#)

*Phys. Plasmas* **13**, 043106 (2006); 10.1063/1.2195383

[Study of intense femtosecond laser propagation into a dense Ar gas and cluster jet](#)

*Phys. Plasmas* **13**, 033105 (2006); 10.1063/1.2180689

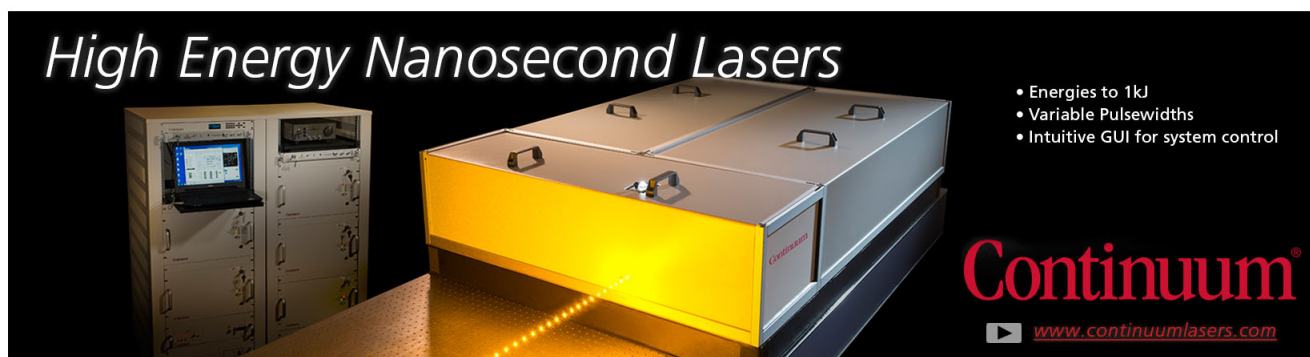
[The interactions of ultra-short high-intensity laser pulses with large molecules and clusters: Experimental and computational studies](#)

*Phys. Plasmas* **8**, 2517 (2001); 10.1063/1.1357829

[Calibration of one-dimensional boosted kinetic codes for modeling high-intensity laser–solid interactions](#)

*Phys. Plasmas* **6**, 947 (1999); 10.1063/1.873335

---

An advertisement for Continuum High Energy Nanosecond Lasers. The image shows a large, industrial-grade laser system with a prominent yellow glow from the laser output. To the left, there is a control console with a monitor and various buttons. The text 'High Energy Nanosecond Lasers' is written in a large, white, serif font at the top left. On the right, there is a list of features: 'Energies to 1kJ', 'Variable Pulseswidths', and 'Intuitive GUI for system control'. The Continuum logo is in a large, red, serif font at the bottom right, with the website 'www.continuumlasers.com' below it.

*High Energy Nanosecond Lasers*

- Energies to 1kJ
- Variable Pulseswidths
- Intuitive GUI for system control

**Continuum**<sup>®</sup>

[www.continuumlasers.com](http://www.continuumlasers.com)

## Revisiting argon cluster formation in a planar gas jet for high-intensity laser matter interaction

Y. Tao,<sup>1</sup> R. Hagmeijer,<sup>2</sup> E. T. A. van der Weide,<sup>2</sup> H. M. J. Bastiaens,<sup>1</sup> and K.-J. Boller<sup>1</sup>

<sup>1</sup>*Laser Physics and Nonlinear Optics, Department of Science and Technology, MESA+ Institute for Nanotechnology, University of Twente, Enschede, The Netherlands*  
<sup>2</sup>*Engineering Fluid Dynamics, University of Twente, Enschede, The Netherlands*

(Received 12 January 2016; accepted 7 April 2016; published online 22 April 2016)

We determine the size of argon clusters generated with a planar nozzle, based on the optical measurements in conjunction with theoretical modelling. Using a quasi-one dimensional model for the moments of the cluster size distribution, we determine the influence of critical physical assumptions. These refer to the surface tension depending on the presence of thermal equilibrium, the mass density of clusters, and different methods to model the growth rate of the cluster radius. We show that, despite strong variation in the predicted cluster size,  $\langle N \rangle$ , the liquid mass ratio,  $g$ , can be determined with high trustworthiness, because  $g$  is predicted as being almost independent of the specific model assumptions. Exploiting this observation, we use the calculated value for  $g$  to retrieve the cluster size from optical measurements, i.e., calibrated Rayleigh scattering and interferometry. Based on the measurements of the cluster size vs. the nozzle stagnation pressure, we provide a new power law for the prediction of the cluster size in experiments with higher values of the Hagena parameter ( $\Gamma^* > 10^4$ ). This range is of relevance for experiments on high-intensity laser matter interactions. © 2016 Author(s). All article content, except where otherwise noted, is licensed under a Creative Commons Attribution (CC BY) license (<http://creativecommons.org/licenses/by/4.0/>). [<http://dx.doi.org/10.1063/1.4947187>]

### I. INTRODUCTION

The formation of the nanometer-sized objects via the van-der-Waals aggregation of gas atoms and molecules, called cluster formation, is emerging into a highly important technique for the field of high-intensity laser-matter interactions.<sup>1</sup> As compared to the standard gas targets made of atomic or molecular monomers, clusters provide a number of unique advantages and novel options. These are, for instance, achieving higher efficiency in THz generation,<sup>2</sup> high-harmonic generation with shorter cut-off wavelengths, reduced saturation and higher yield,<sup>3,4</sup> increased field gradients for laser-driven particle acceleration,<sup>5</sup> or super-hot microplasmas for nuclear fusion.<sup>6</sup>

The advantages mentioned are associated with the relatively large mass and size of clusters, typically thousands to millions of atoms or molecules, which offers a much stronger interaction with the drive laser radiation and allows to form spatially tailored density distributions. Specifically, the periodic density distributions are promising, such as for direct acceleration of particles<sup>7</sup> or quasi-phase matching in high-harmonic generation.<sup>8</sup>

The experimental results obtained with clusters depend, however, critically on the cluster size,  $\langle N \rangle$ , i.e., of the number of constituent atoms per cluster, and, typically, changing global experimental parameters (pressure, temperature) is intended to obtain the clusters of a certain size. An example is the retrieval of structural and dynamical information on sub-nanometer and attosecond scales via high-harmonic generation.<sup>9</sup> Another example is the density contrast that can be obtained in the periodic structuring of the cluster jets, e.g., via an array of wires.<sup>10</sup> Here, a lower temperature in the jet

increases the cluster size and improves the directedness of the flow, whereas the monomer contribution in the flow gives rise to shock waves that reduce the cluster size and the density contrast.

In summary, there is a great need for an easy and reliable method for determining the size of clusters as well as a clear understanding of cluster formation. However, achieving a desired cluster size is problematic. A measurement of the cluster size that has been generated with a certain set of global parameter is difficult due to the highly transient and dynamical character of nanocluster formation.<sup>11,12</sup> Before we present our measurements and improved theoretical modelling of cluster formation, let us recall the current understanding of cluster formation and according models and point to some serious limitations.

Generally, clusters are generated in a supersonic jet expansion. The thermodynamic state of the gas in terms of pressure and temperature typically follows a trajectory through the phase diagram as indicated by the red curve in Figure 1, as was already indicated by, e.g., Hagena.<sup>13</sup> Starting in the high-temperature, the high-pressure region (gas phase) of the gas reservoir, the state initially follows an isentropic change ('dry limit') and then enters the liquid phase region by crossing the saturation curve ('saturation limit') where the pressure,  $p$ , equals the saturation pressure,  $p_s$ , and the nucleation sets in. When the saturation ratio is sufficiently above unity, the nucleation reaches its peak value such that the trajectory starts to deviate from the isentropic curve. The temperature reaches a minimum value at the so-called Wilson-point<sup>14</sup> and thereafter increases again due to latent heat release. At this stage, the nucleation



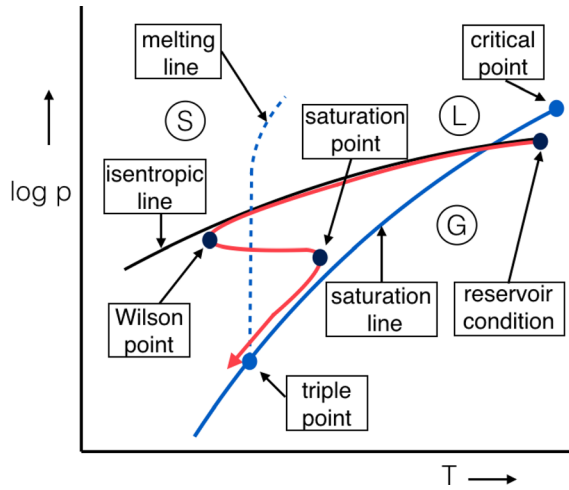


FIG. 1. Typical vapor expansion trajectory in the phase diagram.

rapidly decreases and the cluster growth takes over as the main condensation process. The thermodynamic state proceeds nearly isobarically towards the saturation curve and the temperature reaches a local maximum. From this point onwards, the pressure remains slightly higher than the saturation pressure, while the temperature decreases further.

A problem with the described changes of state is that certain details are not known but can have a large influence. For instance, if the trajectory briefly enters the solid state region, still one would not expect an instantaneous solidification or even crystallization, but rather that the clusters remain liquid in a super-cooled state. Another issue is the validity of assuming a thermal equilibrium between the forming clusters and the remaining gas. The remaining gas might have a lower temperature (due to expansion), while clusters could show a higher temperature caused by the release of latent heat upon growth. Due to the described phase changes and non-equilibrium dynamics involving nanoscale phenomena, an adequate theoretical description can become extremely complex and suffer from large uncertainties.

Nevertheless, the size of the clusters,  $\langle N \rangle$ , is widely assumed to follow a simple power law that has been experimentally observed with an orifice<sup>15</sup>

$$\langle N \rangle = 33 \left( \frac{\Gamma^*}{1000} \right)^{2.35}. \quad (1)$$

In this expression, the main experimental conditions are summarized in the Hagen parameter

$$\Gamma^* = k_h \left( \frac{0.74d}{\tan \alpha} \right)^{0.85} p_o T_o^{-2.29}, \quad (2)$$

where  $k_h$  is a gas-specific constant (for argon,  $k_h = 1650$ ),  $d$  is the diameter of the orifice in  $\mu\text{m}$ ,  $\alpha$  is the expansion half-angle of the jet,  $p_o$  is the stagnation pressure in mbar, and  $T_o$  is the stagnation temperature in K.

The experimental power law observed at an orifice, however, has only been satisfactorily reproduced with the additional experimental data<sup>15</sup> at low gas densities, in a relatively small range of  $1000 < \Gamma^* < 7300$  by time-of-flight

mass spectroscopy, and only with the nozzles having a simple conical symmetry. Nonetheless, the power law is frequently used for evaluating experiments that lie far outside the confirmed range of validity, i.e., at much higher values of the Hagen parameter, also in combination with non-conical geometries. The reason why such extrapolation is still frequently used is that a measurement of  $\langle N \rangle$  is actually not trivial, as can be seen as follows.

To obtain experimental information about  $\langle N \rangle$ , Rayleigh scattering is often applied. However, this method alone does not allow to determine the absolute value of  $\langle N \rangle$  because the absolute strength of the Rayleigh scattering signal,  $I_{RS}$ , is also proportional also to the total atomic number density,  $n_a$ , and the liquid-mass-fraction,  $g$ , which is the ratio of the number of atoms in the form of clusters to the total number of atoms:

$$I_{RS} \propto n_a \langle N \rangle g. \quad (3)$$

In some experiments,<sup>16</sup> the interferometric techniques that yield  $n_a$  were combined with the Rayleigh scattering measurements in order to obtain  $\langle N \rangle$  from  $n_a$  and  $I_{RS}$ , but this requires additional information on  $g$ . Often some *ad hoc* assumptions are made, for instance, by choosing  $g = 1$  without further justification.<sup>17</sup> Other researchers measured the value of  $g$  using Mie scattering from very large clusters (several hundreds of nanometers diameter).<sup>18,19</sup> However, this Mie scattering technique would not be applicable for the much smaller clusters in our work (up to few tens of nanometers diameter).

Recently, Gao *et al.*<sup>20,21</sup> have provided the first independent measurement of  $g$  via recording time-resolved refractive index changes using frequency domain holography during cluster explosion driven by a high-intensity laser. Their measurements yielded an upper limit for  $g$  (e.g.,  $g < 0.5$  at room temperature). Here a problem is that a calculation of the average ionization states of the clusters during the laser cluster interaction is needed, the estimation of which is difficult and less reliable.

An interesting alternative that might give more reliable values for  $g$  is to develop a physical model based on a description of nucleation and growth of clusters (cluster formation). If the model is sufficiently reliable, calculated values of  $g$  can be used in Eq. (3) to extract from the experimental results (Rayleigh scattering and interferometry), the absolute values of the cluster size. Boldarev *et al.*<sup>22,23</sup> have developed a three-dimensional model for the investigation of the cluster formation in a conical gas nozzle. They calculated the typical values of  $g \approx 0.20 - 0.25$  at room temperature. As an argument for reliability in determination of  $g$ , they found good agreement of their calculations of  $n_a$  with the measured values.

Although the described modelling approach seems adequate in those cases, there are also several problems. First of all, the cluster size is extremely sensitive to the surface tension model used. Boldarev *et al.*<sup>23</sup> applied two different surface tension models in their calculation: the model of Sprow and Prausnitz<sup>24</sup> (which is obtained from experiments) and a linear model which is presented without derivation.

Although the linear model for the surface tension differs only slightly (by 16%) from the Sprow and Prausnitz model at the triple-point temperature, the predicted cluster size differs at least an order of magnitude.

Second, the cluster size is also very sensitive to the liquid mass density which can either be taken from the data obtained at saturation conditions<sup>25</sup> or be derived from assuming the solid-like density of a face centered cubic (fcc) lattice.<sup>22</sup> Changing from one model to the other again results in an order of magnitude difference in  $\langle N \rangle$ .

Third, the cluster size is very sensitive to the growth rate of clusters which is cluster-size dependent. In the model applied by Boldarev *et al.*,<sup>23</sup> it is implicitly assumed that  $\langle N \rangle$  is equal to the critical cluster size, i.e., the size for which the Gibbs free energy has a maximum. Variation of the growth rate model in this respect has large implications on the resulting values of  $\langle N \rangle$ .

Finally, the cluster size is very sensitive to the temperature of the clusters during the growth phase. One may either assume that the clusters have the same temperature as the surrounding gas, whereas, as mentioned above, expansive cooling of the gas and release of latent heat during cluster growth suggest that a thermal non-equilibrium model is to be applied.

These uncertainties show that an experimental determination of the cluster size based on the optical measurements requires an improved modelling of cluster formation in search of reliable auxiliary information. Reliable means that this auxiliary information needs to be insensitive to the named variations in modelling as a justification for using it for the evaluation of optical data.

Here, we present a comprehensive modelling of cluster formation and systematically investigate all of the four named sensitivities for the expansion in a supersonic nozzle using argon as an example. Using a model that is based on conservation of mass, momentum, and energy, and which describes the cluster size distribution via its moments, we vary the critical model assumptions. These are, specifically, a thermal equilibrium *vs.* a non-equilibrium surface tension model, a liquid *vs.* a solid-like mass density of the clusters, and a small-cluster and Hill's radius *vs.* a large-cluster limit for the growth rate.

Despite the heavy variations of the cluster size that we observe depending on the model assumptions, we obtain that the liquid-mass fraction,  $g$ , is almost insensitive to the model variations. This strongly supports the validity of our model for a safe determination of  $g$ . Using this information in combination with new measurements based on Rayleigh scattering and interferometry, we derive a new experimental power law that can be used to determine the cluster size from Hagen parameter,  $\Gamma^*$ . The derived power law complements the prediction of the cluster size in the range of at least an order of magnitude higher  $\Gamma^*$  than before ( $1.8 \times 10^4 < \Gamma^* < 2.5 \times 10^5$ ), i.e., well beyond the proven validity of Hagen's relation.

## II. EXPERIMENTS

### A. Experimental setup

To measure the average cluster size,  $\langle N \rangle$ , we have generated an argon cluster jet using a supersonic slit nozzle

(planar nozzle, slit area:  $1.0 \times 5.0 \text{ mm}^2$ , throat size:  $220 \times 900 \mu\text{m}^2$ , expansion half-angle:  $14^\circ$ ) mounted on the top of a solenoid pulsed valve (Parker, 9 series). The nozzle is installed in a vacuum chamber and operates at a repetition rate of 0.25 Hz.

For Rayleigh scattering and interferometric measurements, we have built an experimental setup as shown in Figure 2, comprising a Mach-Zehnder interferometer and a detection of single-pass Rayleigh scattered light. The jet is placed in the upper arm of the interferometer. The slit nozzle can be turned to be positioned either perpendicular or parallel to the laser beam. To measure the total atomic number density distribution in the cluster jet, we inject the interferometer into the beam from a linearly polarized He-Ne laser (wavelength 633 nm). Interference fringes containing information about the density distribution of the jet are imaged onto a CMOS camera (PixeLink, PL-A741) through a lens with a 750 mm focal length.

To quantify the number density and size of clusters via Rayleigh scattering, the beam of a linearly polarized continuous-wave diode pumped solid state laser (DPSSL, operating at 532 nm at an output power of 100 mW) was focused at a distance of 1 mm above the nozzle exit using a lens with a focal length of 20 cm. The nozzle is positioned to be parallel to the laser beam. The Rayleigh range of the beam is around 1 cm. Scattered light from the jet is recorded under an angle of  $90^\circ$  with another camera (pixeLink) equipped with a focal length of 50 mm zoom lens. For a calibration of the Rayleigh scattering signal, scattering from a known density of gas atoms (argon) in the field imaged by the camera was recorded. For this purpose, the entire vacuum chamber was filled with argon gas at a known pressure while keeping the other setup parameters unchanged, specifically, the collection angle, the optical system transmission as well as the gain of the camera. Both cameras and the driver for the gas valve in the experiment are electronically synchronized (Thales, Intelligence Synchronization Electronics for Optics).

In the experiments on cluster formation, the argon gas is supplied to the backside of the valve (and nozzle) with varying stagnation pressures of up to 70 bars. The length of the opening time interval of the valve is set to a sufficiently long value (5 ms) to reach a steady-state flow. Steady-state flow is confirmed by monitoring the scattering signals as a function of time with a photomultiplier at the position of the camera. During repetitive valve operation, the time averaged background pressure lies in a range between  $10^{-3}$  and  $10^{-2}$  mbar depending on the stagnation pressure applied. In order to attain a good signal-to-noise ratio and to reduce the effect of shot-to-shot deviations in the gas flow, all the measurements are averaged over 20 gas shots.

### B. Interferometry

To derive the total atomic number density,  $n_a$ , of argon from the experimental data, we first retrieve the phase information from the interference fringe pattern by using spatial Fourier transformation, high-frequency filtering, and back Fourier transformation.<sup>26</sup> By comparing the phase

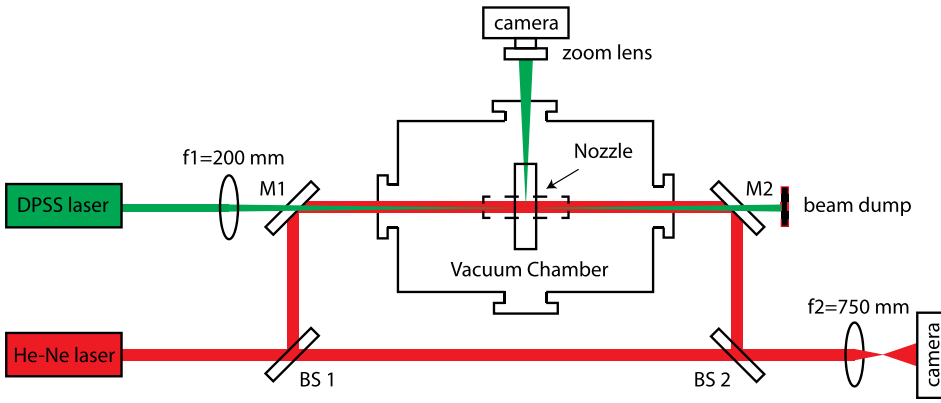


FIG. 2. Schematic of the experimental setup. Red beam path: Mach-Zehnder interferometer; green beam path: beam paths for imaging of Rayleigh scattering. The nozzle can be rotated by  $90^\circ$  (dashed line) for a transverse interferometric measurement.

information when the gas valve is open vs. close, two-dimensional, cross-sectional phase shift distributions,  $\phi$ , are obtained. From the phase shift distributions, we calculate the refractive index distribution,  $n(\lambda)$ , in the cluster jet using

$$\phi = \frac{2\pi}{\lambda} (n(\lambda) - 1) d_{\text{eff}}, \quad (4)$$

where  $\lambda$  is the wavelength of the laser and  $d_{\text{eff}}$  is the effective interaction thickness of the cluster jet as experienced by the laser beam. In order to determine  $d_{\text{eff}}$ , we perform another interferometric measurement of the jet, with the same experimental settings, however, with the nozzle rotated by  $90^\circ$  as indicated by dashed rectangle in Figure 2. The recorded transverse phase shift profile showed near Gaussian shape having a thickness at half maximum (FWHM) of  $d_{\text{eff}} = 0.65$  mm, as obtained by a Gaussian fit. Replacing the Gaussian shape with a homogeneous (rectangular) density distribution of the same area, and by approximating its width,  $d_{\text{eff}}$ , with the FWHM from the fit, we obtain  $n(\lambda)$  via Eq. (4). The total atom number density,  $n_a$ , is then obtained using the Clausius-Mossotti relation

$$n_a = \frac{3\epsilon_o}{\alpha(\lambda)} \left[ \frac{n(\lambda)^2 - 1}{n(\lambda)^2 + 2} \right], \quad (5)$$

where  $\epsilon_o$  is the vacuum permittivity and  $\alpha(\lambda)$  is the atomic polarizability of the respective gas. For argon monomers  $\alpha(633 \text{ nm}) = 18.52 \times 10^{-41} \text{ Fm}^2$ , while the polarizability for argon clusters can be computed<sup>22</sup> as  $\alpha_c = \alpha(\lambda) \langle N \rangle$ .

A typical interference fringe pattern obtained from the cluster jet is shown in Figure 3(a). The presence of the jet can be identified as a slight upward shift of the fringes near the exit of the nozzle as indicated by the arrow. The absolute value of the phase-shift distribution retrieved from the interferogram is presented in Figure 3(b).

Using Eq. (5), we calculate the corresponding total atomic number density,  $n_a$ , and the typical cross sections are shown in Figure 4 where  $n_a$  is plotted versus lateral position along the nozzle exit about 1 mm above the exit for various stagnation pressures. It can be seen that the  $n_a$ -profiles are fairly uniform (maximum  $\sim 10\%$  deviation) with steep gradients near the nozzle walls. Increasing the pressure from 50 to 70 bars leads to an increase in average density from  $7 \times 10^{18}$  to  $10.5 \times 10^{18} \text{ cm}^{-3}$ , while the density profile

remains of approximately the same shape. The absolute values of the densities are sufficiently high to be suitable for typical laser-cluster experiments such as in high-harmonic generation, where comparable densities are used in similar jets.<sup>3-6</sup>

### C. Rayleigh scattering

In the Rayleigh scattering experiments, we performed a series of measurements with stagnation pressures varying from 8 to 70 bars. To remove a spatially uniform background signal, we define the effective area of the scattering region as the area where the scattering intensity is higher than 3% of the maximum intensity in the scattering trace.<sup>27</sup> With this definition, we observe that the size of the scattering region is close to the length of the slit (5.0 mm). The Rayleigh scattering intensity at the camera is quantified as a number of

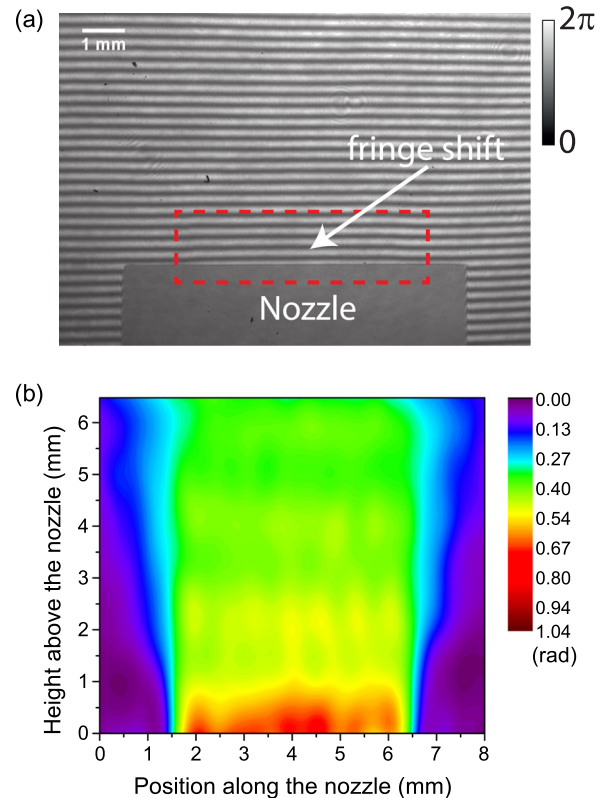


FIG. 3. Interferogram (a) and retrieved phase shift (b) from an argon cluster jet generated at 50 bar stagnation pressure.

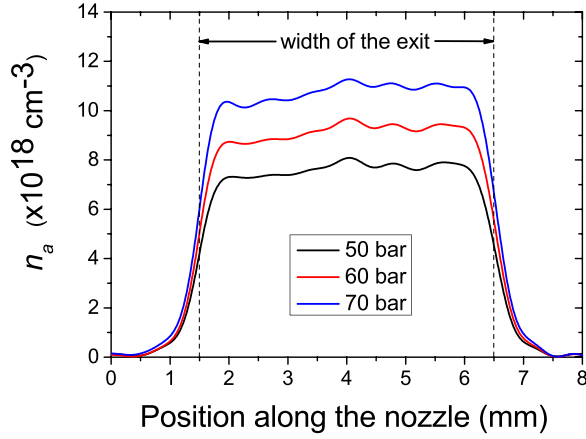


FIG. 4. Measured spatial profile of the total atomic number density,  $n_a$ , in the argon cluster jet about 1 mm above the exit of the nozzle for stagnation pressures of 50, 60, and 70 bars, respectively.

counts per pixel measured within the exposure time interval (5 ms). Across the effective area, the number of counts per pixel is spatially integrated to obtain the total Rayleigh scattering signal,  $I_{RS}$ , which is theoretically equal to<sup>22</sup>

$$I_{RS} = C \alpha_R^2 P_o n_c \langle N^2 \rangle. \quad (6)$$

Here,  $C$  is a constant containing the optical collection angle, wavelength of the scattered light, optical system transmission as well as other efficiency parameters of the CCD camera,  $\alpha_R$  is the atomic polarizability at the used wavelength of 532 nm,  $P_o$  is the incident laser power, and  $n_c$  is the cluster density (the number of clusters per unit volume).

Using the conservation law for the number of atoms,  $n_c \langle N \rangle = g n_a$ , Eq. (6) can be rewritten as follows:

$$I_{RS} = C \alpha_R^2 P_o \Psi g n_a \langle N \rangle, \quad (7)$$

where  $\Psi = \frac{\langle N^2 \rangle}{\langle N \rangle^2} = 1 + \frac{\langle N^2 \rangle - \langle N \rangle^2}{\langle N \rangle^2}$  is the ratio between the averaged squared and the squared average cluster size. By assuming a Gaussian size distribution, Dorchie and co-workers<sup>22,23</sup> estimated that the value of  $\frac{\langle N^2 \rangle - \langle N \rangle^2}{\langle N \rangle^2}$  is typically 20%. In this work, we have used computed values of  $\Psi$ , obtained from the moments of the cluster size distribution as a function of  $\Gamma^*$ . The calculations confirm that  $\Psi$  deviates indeed only marginally from unity. For a determination of the factor  $C \alpha_R^2 P_o$  in Eq. (6), i.e., for an absolute calibration of the Rayleigh scattering signal, we make use of the fact that with the vacuum vessel filled with argon gas, the Rayleigh scattering signal amounts to

$$I_{RS} = C \alpha_R^2 P_o n_a. \quad (8)$$

Here, we determined  $n_a$  via a measurement of the gas pressure which yields for the factor in Eq. (6) an absolute value of

$$C \alpha_R^2 P_o = \frac{I_{RS}}{n_a}. \quad (9)$$

A typical image of Rayleigh scattering at the argon cluster jet about 1 mm above the exit of the nozzle is shown

in Figure 5. The total Rayleigh scattering signal,  $I_{RS}$ , from the jet is plotted in the upper part of Figure 6 as a function of the nozzle stagnation pressure. In the lower part of Figure 6, the Rayleigh scattering signal,  $I_{RS}$ , vs. the static pressure from the calibration experiment in argon gas is plotted. The value of the factor  $C \alpha_R^2 P_o$  derived from the calibration experimental data via a linear fit (red line in lower part of Figure 6) is

$$C \alpha_R^2 P_o = 1.32 \pm 0.19 \times 10^{-17} \text{ counts/cm}^3. \quad (10)$$

Looking at Eq. (7), for a determination of the cluster size,  $\langle N \rangle$ , additional information on the liquid mass fraction,  $g$ , and the ratio between the averaged squared and the squared average cluster size,  $\Psi$ , is required. In the following, we present a quasi-one dimensional model to calculate  $g$  and  $\Psi$ . Special emphasis is put on an evaluation of the variation of the theoretical predictions when varying the critical physical assumptions. In spite of heavy variations of the cluster size by several orders of magnitude, we observe that  $g$  remains almost insensitive to variations in the model, which makes it possible to predict  $g$  safely.

### III. THEORETICAL MODEL

#### A. Nozzle geometry and reservoir conditions

We consider our planar nozzle as depicted in Figure 7 which is described in terms of an axial coordinate  $x$ , with  $x=0$  at the throat, and cross section  $A(x)$ . The nozzle has a constant width of  $w=0.9$  mm along the  $x$  axis, a throat height of  $h_o=0.22$  mm, a half-angle of  $\alpha=0.244$  rad ( $14^\circ$ ), and a length of  $L_N=10$  mm. The cross section,  $A$ , is then given by

$$A(x) = h(x)w, \quad h(x) = h_o + 2x \tan \alpha. \quad (11)$$

The reference reservoir conditions chosen in this work in terms of pressure and temperature are  $p_o^{\text{ref}} = 50$  bar and  $T_o^{\text{ref}} = 293$  K, respectively. Both parameters have been varied individually while keeping the other variable constant as shown in Table I.

#### B. Conservation equations

The conservation equations for mass, momentum, and energy in quasi-one dimensional flow with negligible viscosity and heat conduction can be written as

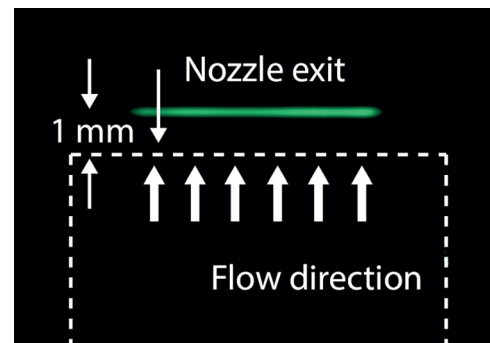


FIG. 5. A typical Rayleigh scattering image of argon clusters about 1 mm above the nozzle at a stagnation pressure of 70 bars.

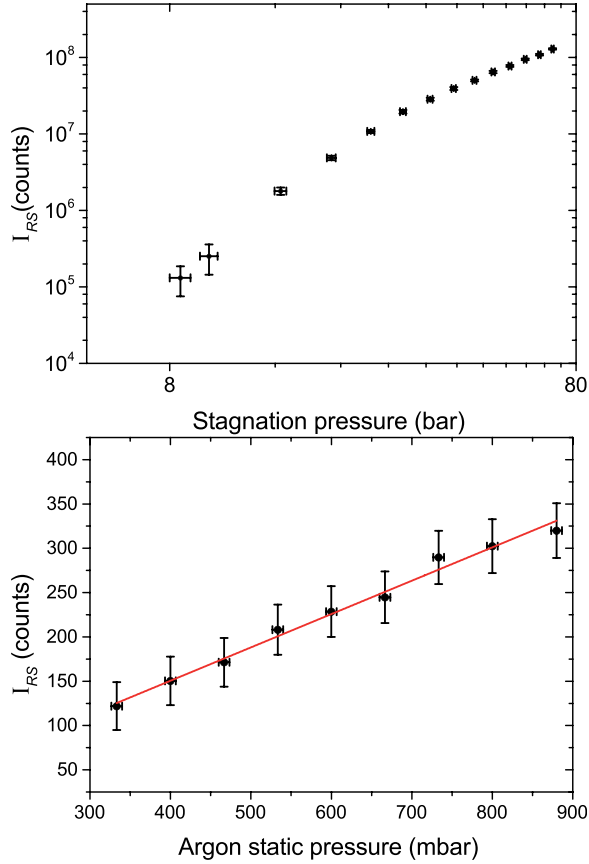


FIG. 6. Rayleigh scattering signals from the argon cluster jet (top) and from the calibration experiment in static argon gas (bottom) and the error bars in both figures indicate the standard deviation of the Rayleigh scattering intensity from pixel to pixel for each measurement. The red line is a linear least-square fit to determine the calibration factor  $C \alpha_R^2 P_o$ .

$$\frac{D}{Dt}(\rho u A) = 0, \quad (12)$$

$$\frac{Du}{Dt} = -\frac{1}{\rho} \frac{Dp}{Dt}, \quad (13)$$

and

$$\frac{DH}{Dt} = 0, \quad (14)$$

where  $\rho$  and  $u$  are the mass density and velocity of the vapor-clusters mixture,  $p$  is the vapour pressure,  $H$  is the total specific enthalpy, and  $\frac{D}{Dt}$  is the material derivative which in case of stationary flow is defined as

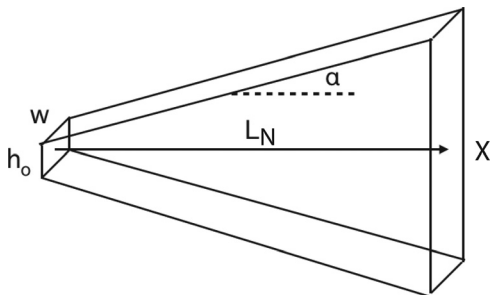


FIG. 7. Geometry of the planar nozzle used for modelling and in the experiments.

TABLE I. Definition of the pressure and temperature series.

Pressure series	
$p_o = 10, 20, 30, \dots, 100 \text{ bar}$	$T_o = T_o^{\text{ref}}$
Temperature series	
$p_o = p_o^{\text{ref}}$	$T_o = 200, 215, 230, \dots, 350 \text{ K.}$

$$\frac{D}{Dt} \equiv u \frac{\partial}{\partial x}. \quad (15)$$

The total specific enthalpy is defined as

$$H \equiv e + \frac{1}{2}u^2 + \frac{p}{\rho}, \quad (16)$$

where  $e$  is the internal specific energy. Combination of Eqs. (13), (14), and (16) leads to

$$\frac{De}{Dt} - \frac{p}{\rho^2} \frac{D\rho}{Dt} = 0, \quad (17)$$

which shows that the flow is isentropic in the case when there is no phase transition.

To relate the thermodynamic variables to each other, we use the thermal equation of state

$$p = (1 - g)z(\rho, T)\rho RT \quad (18)$$

and the calorical equation of state

$$e = c_v T + gRT - gL, \quad (19)$$

where  $g$  is the liquid mass fraction,  $z(\rho, T)$  is the compressibility factor (detailed description is presented in the Appendix),  $R$  is the specific gas constant,  $T$  is temperature,  $c_v$  is the specific heat at constant volume, and  $L$  is the latent heat.

To model the formation of clusters as a distribution of clusters of various different sizes, we introduce the distribution function,  $f(r)$ , where  $r$  is the cluster radius. The spatiotemporal development of  $f(r)$  is described via its moments which are integrals over the cluster-radius distribution function

$$\hat{\mu}_k = \mu_k / \rho, \quad \mu_k = \int_0^\infty f(r)r^k dr. \quad (20)$$

The moment  $\hat{\mu}_0$  represents the number of clusters per unit mass and  $\hat{\mu}_3$  is related to the liquid mass fraction, i.e., the amount of liquid mass per unit mass of the mixture

$$g = \frac{4}{3}\pi\rho_L\hat{\mu}_3, \quad (21)$$

with  $\rho_L$  the bulk mass density of the liquid phase. Finally, we calculate  $\Psi$  from the ratio of moments ( $\hat{\mu}_0$ ,  $\hat{\mu}_3$ , and  $\hat{\mu}_6$ )

$$\Psi \equiv \frac{\langle N^2 \rangle}{\langle N \rangle^2} = \frac{\hat{\mu}_0 \hat{\mu}_6}{\hat{\mu}_3^2}. \quad (22)$$

The moments satisfy the following transport equations:<sup>28–30</sup>

$$\frac{D\hat{\mu}_k}{Dt} = \hat{J}r_*^k + k\langle \dot{r} \rangle \hat{\mu}_{k-1}, \quad k = 0, 1, 2, 3, \quad (23)$$

where  $\hat{J}$  is the classical nucleation rate per unit mass,  $r_*$  is the critical radius, and  $\langle \dot{r} \rangle$  is a suitable chosen average of the

radius-dependent cluster growth rate (see Section III E). We basically follow the classical nucleation theory as given in, e.g., Refs. 31 and 32, where the nucleation rate is modeled as

$$\hat{J} = J/\rho, \quad J = K \exp\left(-\frac{\Delta G_*}{k_B T}\right). \quad (24)$$

Here,  $\Delta G_*$  is the critical value of the Gibbs free energy of formation

$$\Delta G_* = \frac{4}{3}\pi r_*^2 \sigma, \quad (25)$$

with  $\sigma(T)$  is the surface tension, and  $K$  is the prefactor

$$K = \frac{\rho_1^2}{\rho_L} \sqrt{\frac{2\sigma}{\pi m_1^3}}, \quad (26)$$

with  $\rho_1 = (1-g)\rho$  is the monomer density,  $\rho_L$  is the bulk density of the liquid phase, and  $m_1$  is the monomer mass.

The Gibbs free energy of formation attains its critical value at the critical radius

$$r_* = \frac{2\sigma}{\rho_L R T \ln S}, \quad (27)$$

where  $S$  is the saturation ratio, i.e., the ratio between the vapor pressure  $p$  and the saturated vapor pressure  $p_s(T)$

$$S = \frac{p}{p_s(T)}. \quad (28)$$

Finally, the growth rate is modeled by the Hertz-Knudsen growth law

$$\dot{r} = \frac{\beta}{\rho_L} \left( \frac{p}{\sqrt{2\pi R T}} - \frac{p_{s,r}}{\sqrt{2\pi R T_{cl}}} \right), \quad (29)$$

where  $\beta$  is the sticking probability,  $T_{cl}$  is the cluster temperature, and  $p_{s,r}$  is the saturated vapor pressure over a curved surface with radius  $r$

$$p_{s,r} = p_s \exp\left(\frac{r_*}{r} \ln S\right) = p S^{r_* r^{-1}}. \quad (30)$$

The sticking probability in this work is taken as  $\beta = 1$ . We are aware that this choice somewhat affects the average cluster size and liquid mass fraction, see, e.g., a sensitivity analysis by Sidin *et al.*,<sup>33</sup> but there is a lack of a clear argument to assume another value.

The complete set of equations is solved using the method presented in the Appendix.

### C. Surface tension model

To model the surface tension for argon, the gas that is used in our experiments, we make use of the model of Sprow and Prausnitz:<sup>24</sup>

$$\sigma(T) = \sigma_o \left(1 - \frac{T}{T_c}\right)^c, \quad (31)$$

where  $T_c$  is the critical temperature and

$$\sigma_o = 37.78 \times 10^{-3} \text{N/m}, \quad c = 1.277. \quad (32)$$

We will refer to a first model as the **thermal equilibrium surface tension model** by assuming that the cluster temperature remains equal to the gas temperature via a sufficiently fast heat transfer.

The critical value of the Gibbs free energy of formation depends cubically on surface tension,

$$\ln(J/K) \sim \sigma^3. \quad (33)$$

Upon neglecting high order variations of  $K$  with  $\sigma$  as an approximation, one finds the following estimate for the dependence of the nucleation rate on the surface tension,  $\sigma$ :

$$\frac{J + \Delta J}{J} \approx \left(\frac{J}{K}\right)^{3\Delta\sigma/\sigma}. \quad (34)$$

At the nucleation peak one typically has  $J/K \approx 10^{-14}$ , which, already for a small variation of surface tension, e.g.,  $\Delta\sigma/\sigma = \pm 10\%$ , leads to a large variation of  $(J + \Delta J)/J$  by approximately four orders of magnitude.

A further uncertainty is the following. When the pressure and the temperature enter the solid phase regime, clusters will tend to change from the liquid phase to the solid phase rendering Eq. (31) formally invalid, or the clusters remain in a liquid, super-cooled phase. As we do not have reliable information on the surface tension at that point in the trajectory, here we assume that the clusters remain liquid, and we take the option of a solid state into account in a later step.

In our second model which we refer to as the **thermal non-equilibrium surface tension model**, we assume that the heat transfer rate between clusters and the gas phase may be relatively low compared to the expansion rate. Next, we will estimate the relative values of these rates, and the estimation suggests that the clusters have a higher temperature than the surrounding gas phase. To model this thermal non-equilibrium effect to some basic extent, the following modification of Eq. (31) is proposed:

$$\sigma(T) = \begin{cases} \sigma_o \left(1 - \frac{T}{T_c}\right)^c, & T \geq T_s, \\ \sigma_o \left(1 - \frac{T_s}{T_c}\right)^c, & T < T_s, \end{cases} \quad (35)$$

where the saturation temperature  $T_s(p)$  is implicitly defined by

$$p_s(T_s(p)) = p. \quad (36)$$

### D. Liquid mass density model

The critical value of the Gibbs free energy of formation depends inversely quadratically on the liquid mass density

$$\ln(J/K) \sim \rho_L^{-2}. \quad (37)$$

Upon neglecting again the variation of  $K$  with  $\rho_L$ , one finds the following estimate for a variation of the nucleation rate vs. a variation of  $\rho_L$ :

$$\frac{J + \Delta J}{J} \approx \left(\frac{J}{K}\right)^{-2\Delta\rho_L/\rho_L}. \quad (38)$$

Again at the typical value  $J/K \approx 10^{-14}$  with only a small variation of the liquid mass density of  $\Delta\rho_L/\rho_L = \pm 10\%$ , one finds a strong variation of  $(J + \Delta J)/J$  by approximately three orders of magnitude.

Two different models for the bulk density are considered. As the first model, the density at the saturation line is used<sup>25</sup>

$$\rho_L^s(T) = \rho_c \exp\left(\sum_{i=1}^4 \rho_i \left(\frac{T}{T_c}\right)^{c_i}\right), \quad (39)$$

where  $\rho_c$  is the critical density and the coefficients  $\rho_i$  and  $c_i$  are given in Table II.

To take a possible solidification of clusters into account, we used, as a second model, the fcc packed bulk density of the solid phase<sup>22</sup>

$$\rho_L^{fcc} = \frac{3}{4}\pi \frac{m_1}{v_o}, \quad v_o = 9.0 \times 10^{-30} \text{ m}^3. \quad (40)$$

The ratio of the mass densities as given by the two assumptions is depicted in Figure 8. It can be seen that there is, particularly at the critical temperature, a significant difference in the mass density and, correspondingly, a large difference in the nucleation rate might be expected.

### E. Growth rate model

The growth rate equation (Eq. (29)) for the radius of a cluster can be rewritten by using Eq. (30),

$$\dot{r} = \frac{\beta}{\rho_L} \left(1 - S_r^{r_*-1} \sqrt{\frac{T}{T_{cl}}}\right) \frac{p}{\sqrt{2\pi RT}}, \quad (41)$$

showing that the growth rate depends nonlinearly on the radius and the cluster temperature. An average growth rate,  $\langle \dot{r} \rangle$ , can be obtained by replacing the cluster radius,  $r$ , and the cluster temperature,  $T_{cl}$ , by suitable average values as follows.

For the cluster temperature,  $T_{cl}$ , two limiting cases are considered: the **thermal equilibrium limit**,

$$T_{cl} \rightarrow T, \quad (42)$$

and the thermal non-equilibrium limit,

$$T_{cl} \rightarrow T_s, \quad (43)$$

TABLE II. Coefficients in liquid mass density Eq. (39).

$i$	$\rho_i$	$c_i$
1	1.5004262	1/3
2	-0.31381290	2/3
3	0.086461622	7/3
4	-0.041477525	4

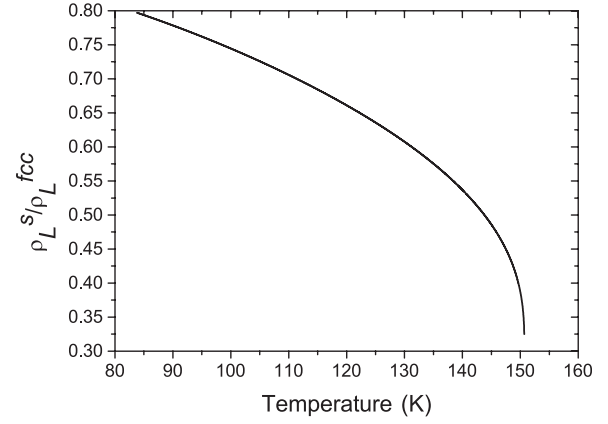


FIG. 8. Liquid mass density ratio,  $\rho_L^s(T)/\rho_L^{fcc}$ , as a function of temperature,  $T$ , with  $T_r < T < T_{cr}$ .

where  $T_s$  is chosen according to the surface tension modification given in Eq. (35).

For the average cluster radius,  $\langle r \rangle$ , three models are considered: the small cluster limit, the so-called Hill's radius, and the large cluster limit. The **small cluster limit** for thermal equilibrium is defined as

$$\frac{\langle r \rangle}{r_*} = 2 \Rightarrow S_r^{r_*-1} \rightarrow 1/\sqrt{S} \quad (44)$$

and for thermal nonequilibrium as

$$\frac{\langle r \rangle}{r_*} = 1 \Rightarrow S_r^{r_*-1} \rightarrow 1. \quad (45)$$

It is noted that taking  $\langle r \rangle/r_* = 1$  in Eq. (44) would lead to a zero growth rate reflecting the maximum in the Gibbs free energy. In the intermediate model by Hill,<sup>28</sup> the average radius is taken as **Hill's radius**:

$$\langle r \rangle = r_H \equiv \sqrt{\frac{\hat{\mu}_2}{\hat{\mu}_o}}, \quad (46)$$

which means that the average value is obtained from the moments of the calculated size distribution function. The **large cluster limit** finally is taken as

$$\frac{\langle r \rangle}{r_*} \rightarrow \infty \Rightarrow S_r^{r_*-1} \rightarrow S^{-1}. \quad (47)$$

### F. Model variation sensitivity

The average cluster size,  $\langle N \rangle$ , is inversely proportional to the liquid mass fraction,  $g$  (see Eq. (7)). The approach taken in this work investigates the sensitivity of the liquid mass fraction with respect to variations of the model. We begin the investigations with a specific choice of model which we call the baseline model (Section III G) because this choice appears to be justified best based on the physical arguments. We will show below that both the average cluster size,  $\langle N \rangle$ , and the cluster number density,  $n_c$ , are extremely sensitive to the variation of the model. However, their

product,  $n_c \langle N \rangle = gn_a$ , turns out to be very insensitive because both  $g$  and  $n_a$  are insensitive, specifically, when the physically more justified thermal non-equilibrium assumption is used.

The average cluster size,  $\langle N \rangle$ , computed under variation of models as described above is depicted in Figure 9 as a function of the Hagen parameter,  $\Gamma^*$ . The top figure shows the results obtained with the thermal equilibrium models and the bottom figure shows the results obtained with the thermal non-equilibrium models. It is evident that the results are extremely sensitive to model variations because they lead to differences of up to eight orders of magnitude. This proves that modelling  $\langle N \rangle$  using any of the assumptions mentioned will not provide trustworthy predictions. Even when not comparing absolute values of  $\langle N \rangle$  but looking only at the variation of  $\langle N \rangle$  with  $\Gamma^*$ , rather different trends are predicted by different groups of models. Specifically, the thermal equilibrium models roughly show an opposite trend than non-equilibrium models in that they predict a decreasing cluster size with increasing  $\Gamma^*$  instead of an increasing cluster size. Such opposite trend can also be observed in the work of Boldarev *et al.*<sup>23</sup> Of all the thermal non-equilibrium models, the model with Hill's radius predicts the largest average cluster size, since it produces the largest growth rate (see Eq. (41)).

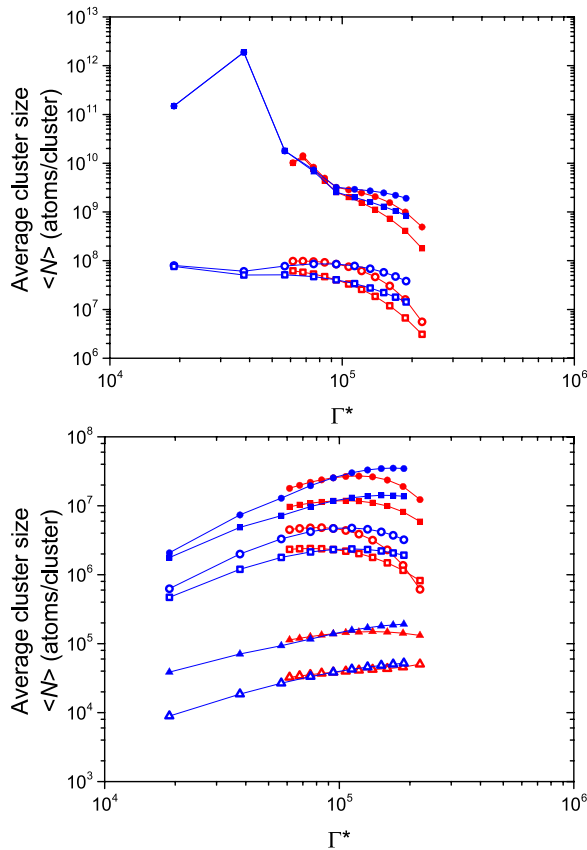


FIG. 9. Computed cluster size as a function of the Hagen parameter at the exit of the nozzle assuming either thermal equilibrium (top, Eqs. (31) and (42)) or thermal non-equilibrium (bottom, Eqs. (35) and (43)) with either super-cooled liquid clusters,  $\rho_L = \rho_L^\xi$  (open symbols), or perfectly crystalline solid density cluster,  $\rho_L = \rho_L^{fcc}$  (closed symbols), assuming various average radii: O:  $\langle r \rangle = r_H$ ,  $\square$ :  $\langle r \rangle = 2r_*$ ,  $\triangle$ :  $\langle r \rangle = r_*$ , either as a variation of the nozzle pressure (blue symbols) or as a variation of the nozzle temperature (red symbols).

The corresponding computational results for the liquid mass fraction,  $g$ , are depicted in Figure 10. Again, the top figure shows the results obtained with the thermal equilibrium models and the bottom figure with the thermal non-equilibrium models. Variations of the thermal equilibrium models lead to considerable variations in  $g$  and even may lead to no nucleation at all (lowest value of  $\Gamma^*$ , small cluster limit with *fcc*-packed density). In contrast, the bottom figure of Figure 10 reveals that  $g$  is *very insensitive* to variations within all thermal non-equilibrium modelling and Figure 10 is therefore a *key figure* in this work. The insensitivity of  $g$ , for thermal non-equilibrium models, together with our time-scale estimation that suggests the presence of thermal non-equilibrium cluster formation (Section III G), supports the conclusion that our model predicts physically correct and reliable liquid mass fraction. This reliability in determining  $g$  is what justifies to make use of the calculated  $g$ -values for deriving the average cluster size from the optical measurements.

The corresponding computational results for the cluster number density,  $n_c$ , are depicted in Figure 11, with again the thermal equilibrium results in the top figure. It can be seen that the sensitivity of  $n_c$  to model variations is as large as the sensitivity of  $\langle N \rangle$ . However, the variations occur in the opposite direction such that the product,  $n_c \langle N \rangle$ , is fairly

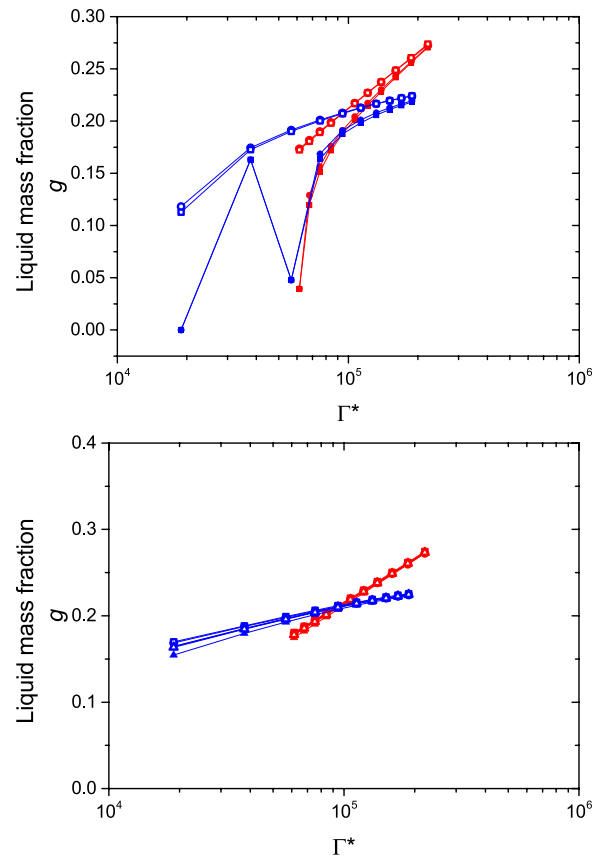


FIG. 10. Liquid mass fraction as a function of the Hagen parameter at the exit of the nozzle assuming either thermal equilibrium (top, Eqs. (31) and (42)) or thermal non-equilibrium (bottom, Eqs. (35) and (43)) with either super-cooled liquid clusters,  $\rho_L = \rho_L^\xi$  (open symbols), or perfectly crystalline solid density cluster,  $\rho_L = \rho_L^{fcc}$  (closed symbols) with various average radii: O:  $\langle r \rangle = r_H$ ,  $\square$ :  $\langle r \rangle = 2r_*$ ,  $\triangle$ :  $\langle r \rangle = r_*$ , either as a variation of the nozzle pressure (blue symbols) or as a variation of the nozzle temperature (red symbols).

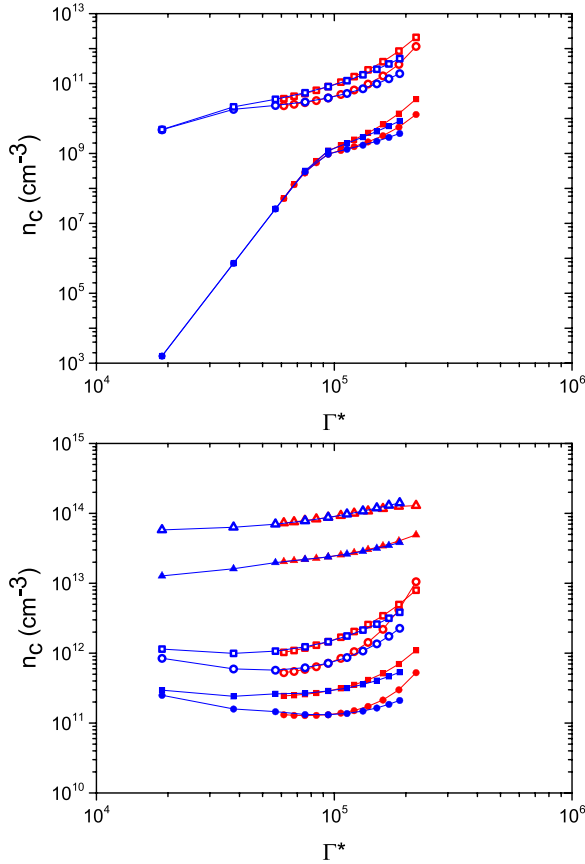


FIG. 11. Cluster number density as a function of the Hagen parameter at the exit of the nozzle assuming either thermal equilibrium (top, Eqs. (31) and (42)) or thermal non-equilibrium (bottom, Eqs. (35) and (43)) with either super-cooled liquid clusters,  $\rho_L = \rho_L^s$  (open symbols), or perfectly crystalline solid density cluster,  $\rho_L = \rho_L^{fcc}$  (closed symbols) with various average radii: O:  $\langle r \rangle = r_H$ ,  $\square$ :  $\langle r \rangle = 2r_*$ ,  $\triangle$ :  $\langle r \rangle = r_*$ , either as a variation of the nozzle pressure (blue symbols) or as a variation of the nozzle temperature (red symbols).

insensitive, and even very insensitive when only thermal non-equilibrium model variations are considered. This is also reflected in Figure 12 where the computational results for the total atom number density are depicted, with the thermal equilibrium models in the top figure and the thermal non-equilibrium models in the bottom figure. Except for the thermal equilibrium small cluster limit with *fcc*-packed liquid mass density, all models give near identical results for  $n_a$ .

### G. Baseline model and results

Among the variation of different choices between possible submodels, we have selected a specific model based on physical arguments which we call baseline model. To choose between the thermal equilibrium and nonequilibrium models, we compare the thermal relaxation time scale of the clusters,  $\tau_r$ , with the convection time scale of the gas flow,  $\tau_f$ . If the thermal relaxation of the clusters is much slower, this would indicate thermal non-equilibrium. We start the comparison with estimating the impingement rate  $\nu$ , i.e., the number of collisions of atoms with a cluster per unit time and per unit area<sup>31</sup>

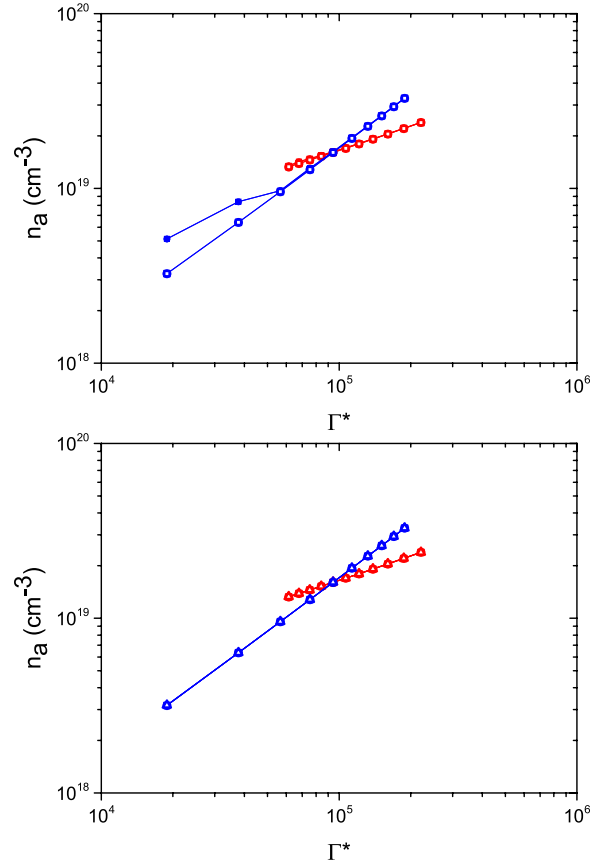


FIG. 12. Total atom number density as a function of the Hagen parameter at the exit of the nozzle assuming either thermal equilibrium (top, Eqs. (31) and (42)) or thermal non-equilibrium (bottom, Eqs. (35) and (43)) with either super-cooled liquid clusters,  $\rho_L = \rho_L^s$  (open symbols), or perfectly crystalline solid density cluster,  $\rho_L = \rho_L^{fcc}$  (closed symbols) with various average radii: O:  $\langle r \rangle = r_H$ ,  $\square$ :  $\langle r \rangle = 2r_*$ ,  $\triangle$ :  $\langle r \rangle = r_*$ , either as a variation of the nozzle pressure (blue symbols) or as a variation of the nozzle temperature (red symbols).

$$\nu = \frac{p}{\sqrt{2\pi m_1 k_B T}}, \quad (48)$$

which has the same order of magnitude as

$$\nu_o = \frac{p_o}{\sqrt{2\pi m_1 k_B T_o}}. \quad (49)$$

Assuming, as an approximation, that the condensation rate and that evaporation rate on a cluster are proportional to each other, and taking again  $\beta = 1$ , the energy per unit time removed from a cluster is

$$\dot{e}_N = \nu_o A_N \frac{3}{2} k_B (T_d - T), \quad (50)$$

where  $N$  is the size of the cluster,  $A_N$  is its surface area, and  $T_d - T$  is the temperature difference between the cluster and the surrounding gas vapor. The thermal relaxation time scale can be now defined as the time needed for  $N$  collisions because a number of  $N$  collisions (each collision associated with sticking and reevaporation of one atom) would lead to equal cluster and vapor temperatures

$$\tau_{r,N} = \frac{N}{\nu_o A_N}. \quad (51)$$

The convection time scale, on the other hand, is taken as the time needed to pass through the nozzle with the speed of sound at stagnation conditions

$$\tau_f = \frac{L}{\sqrt{\gamma RT_o}}. \quad (52)$$

For the reference conditions already for the smallest clusters predicted by theory, i.e., and  $N \approx 10^4$ , we find that the ratio  $\tau_f/\tau_r$  is rather small on the order of  $10^{-3}$ . This estimate indicates that the thermal relaxation is much slower than the convection such that the cluster temperature is expected to be different (higher) than the surrounding vapor temperature. This is why we choose the thermal non-equilibrium options in the surface tension model and in the growth law for our baseline model.

With the same reasoning of relatively slow heat transfer to the clusters, in the baseline model, we take the liquid mass density as equal to the saturation liquid mass density instead of the solid-state *fcc*-packed density. In some of the computations, the thermodynamic state of the vapor does enter the solid state region but in view of the time needed for clusters to relatively lay over their temperature to that of the vapor, we assume that the clusters remain liquid; i.e., liquid mass density is maintained.

The growth law (Eq. (41)) is radius dependent, and as an approximation, we evaluate the growth for a representative average radius. With our model, which provides the moments of the cluster radius distribution, we decided to calculate the average radius from measurements according to Eq. (46) (i.e., we calculate Hill's radius). This corresponds to selecting again thermal non-equilibrium model based on the quantified physical arguments in order to avoid the less justified assumptions on the cluster size, such as the small or large cluster limits. In summary, our baseline model comprises:

- (1) thermal non-equilibrium surface tension model, Eq. (35),
- (2) saturated liquid density model, Eq. (39),
- (3) non-equilibrium cluster temperature, Eq. (43), and
- (4) Hill's average cluster radius, Eq. (46).

The results of the baseline model in terms of average cluster size,  $\langle N \rangle$ , and liquid mass fraction,  $g$ , are depicted in Figure 13 for the pressure series (blue symbols) and the temperature series (red symbols). It is observed that the computed values for the average cluster size from the pressure series and the temperature series have a fair amount of overlap, indicating that the Hagen parameter,  $\Gamma^*$ , indeed approximately covers both the dependence on stagnation pressure and the dependence on stagnation temperature. There is overlap at a single point also for the liquid mass fraction, but the variation shows two slightly different power laws. The liquid mass fraction varies in between 16% and 22% which is consistent with the range reported by Gao *et al.*<sup>21</sup> and Dorchie *et al.*<sup>22</sup>

#### IV. AVERAGE CLUSTER SIZE

By using the liquid mass fraction,  $g$ , and the ratio between the averaged squared and the squared average cluster size,  $\Psi$ ,

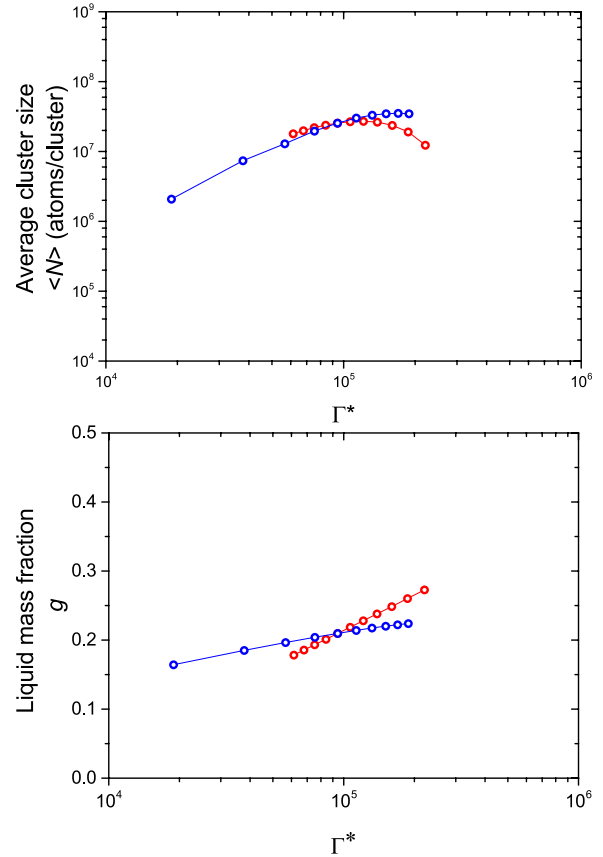


FIG. 13. Average cluster size and liquid mass fraction computed with the baseline model at a constant  $T_o = T_{ref}$  and varying  $p_o$  (blue symbols) and a constant  $p_o = p_{ref}$  and varying  $T_o$  (red symbols).

as obtained from calculations (using the baseline model) as explained in Section III G and shown in Figure 13, an expression for retrieving the average cluster size from optical data can be derived from Eq. (6)

$$\langle N \rangle = \frac{I_{RS}}{C \alpha_R^2 \Psi P_o g n_a}. \quad (53)$$

Inserting in this expression the experimentally determined parameters ( $I_{RS}(p_o)$ ,  $n_a(p_o)$ ) and the calibration factor ( $C \alpha_R^2 P_o$ ), we obtain the relationship between the measured average cluster size,  $\langle N \rangle$ , and the calculated Hagen parameter,  $\Gamma^*$ . In a double logarithm plot, which is shown in top Figure 14, the measured relation between  $\langle N \rangle$  and  $\Gamma^*$  is plotted as black round symbols. For a convenient use in experiments, these data can be represented by a closed algebraic expression obtained by a fit to the data, in the form of a simple power law with a slight linear variation of the exponent

$$\langle N \rangle = 10^{-2.16} \left( \frac{\Gamma^*}{1000} \right)^{7.64 - 1.60 \log \left( \frac{\Gamma^*}{1000} \right)}. \quad (54)$$

It can be seen that, besides a relatively small offset (about one order of magnitude), compared to the variation up to seven orders of magnitude calculated with other models, the data are in good agreement with the measurements. Especially, the trends of the experimental values (black

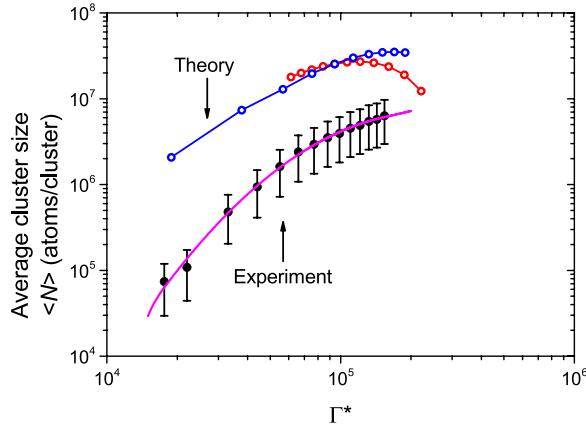


FIG. 14. Average cluster size from the argon cluster jet vs. the Hagena parameter in a double logarithmic plot. The black symbols are derived from optical measurements making use of the calculated, model-insensitive liquid mass ratio,  $g$ . The error bars are calculated from the error bars obtained in the Rayleigh scattering measurement. The pink solid curve is the corresponding parabolic fit line (Eq. (54)). The blue and red symbols are the data calculated from our baseline model.

symbols) and computed values of  $\langle N \rangle$  vs.  $\Gamma^*$  (blue symbols) are very similar.

## V. CONCLUSION

We have investigated argon cluster formation in a planar nozzle expansion both experimentally and theoretically with a main interest in the average cluster size,  $\langle N \rangle$ . The average cluster size at a small distance downstream of the nozzle exit has been determined by combining Rayleigh scattering and interferometry data, on the one hand, and theoretically derived values for the liquid mass fraction, on the other hand, as a function of the so-called Hagena parameter,  $\Gamma^*$ .

The baseline theoretical model employed uses a thermal non-equilibrium surface tension model, a saturated liquid density, a non-equilibrium cluster temperature, and Hill's average cluster radius which is computed from the moments of the size distribution. The liquid mass fraction that is obtained from the base line model proves very insensitive with regard to model variations which justifies the usage of these data to translate measured data to average cluster size. By using our baseline model to calculate the liquid mass fraction,  $g$ , and using  $g$  to retrieve from interferometry and Rayleigh scattering measurements, the average cluster size,  $\langle N \rangle$ , in the region of the higher Hagena parameter,  $\Gamma^*$ , which is well beyond what is known for small cluster from Hagena's guideline.<sup>15</sup> This is summarized in Figure 15 where our experimental data (pink symbols) represented by a modified power law (Eq. (54), pink curve) and our theoretical data (blue and red symbols) are plotted for the range of large values ( $1.5 \times 10^4 < \Gamma^* < 2.5 \times 10^5$ ) in the same graph as Hagena's guideline for lower values across the verified region ( $10^3 < \Gamma^* < 7.3 \times 10^3$ , black line). It can be seen that our power law complements the previously found variation in a consistent fashion and extends the total range of conveniently predictable cluster size from  $\Gamma^* = 10^3$  to  $2.5 \times 10^5$ . Thereby, the extended range of predictable average cluster size,  $\langle N \rangle$ , covers the values from about a thousand to almost ten million

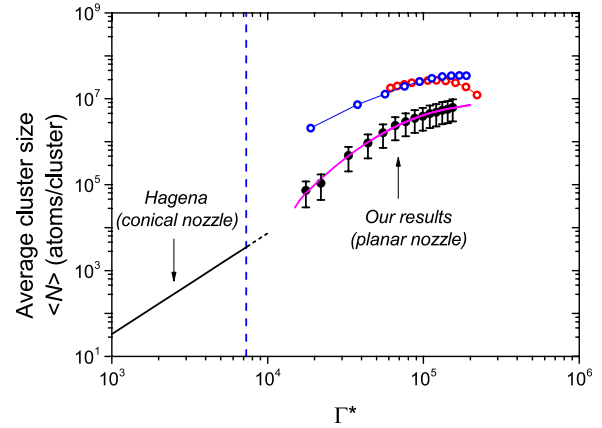


FIG. 15. Average cluster size from the argon cluster jet at different values of the Hagena parameter in a double logarithmic plot. The black symbols are derived from the optical experiments making use of the calculated values of  $g$  as summarized by our modified power law (Eq. (54), pink curve). The blue and red symbols are the data calculated from our baseline model. In the region of lower  $\Gamma^*$  ( $1000 < \Gamma^* < 7300$ ), the solid line displays Hagena's guideline.

atoms per cluster. Further increasing the detection sensitivity in the optical measurements, such as increasing the laser power to the 10-W level, seems promising for establishing a unified experimental power law spanning the entire data range. Towards further increased densities, the cluster sizes appears to approach some limiting size or much slower growth which might be explored with further increased stagnation pressures.

## ACKNOWLEDGMENTS

This research was supported by the Dutch Technology Foundation STW, which is part of the Netherlands Organization for Scientific Research (NWO), and partly funded by the Ministry of Economic Affairs (Project No. 10759).

## APPENDIX: SOLUTION METHOD

Using the equations of state, Eqs. (18) and (19), the material derivatives of  $p$  and  $e$  become

$$\frac{Dp}{Dt} = -\frac{\rho^2}{1-g}\beta_\rho \frac{Dg}{Dt} + \rho\beta_\rho \frac{D\rho}{Dt} + \rho\beta_T \frac{DT}{Dt} \quad (\text{A1})$$

and

$$\frac{De}{Dt} = (c_v + gR) \frac{DT}{Dt} + (RT - L) \frac{Dg}{Dt}, \quad (\text{A2})$$

where

$$\beta_\rho = \frac{1}{\rho} \left[ \frac{p}{\rho} + (1-g) \frac{p}{z} \left( \frac{\partial z}{\partial \rho} \right)_T \right], \quad (\text{A3})$$

$$\beta_T = \frac{1}{\rho} \left[ \frac{p}{T} + \frac{p}{z} \left( \frac{\partial z}{\partial T} \right)_\rho \right]. \quad (\text{A4})$$

The compressibility factor  $z(\rho, T)$  is computed by employing the series expansion described by Reid *et al.*<sup>34</sup>

TABLE III. Coefficients in the second and the third virial coefficients.

$l$	$B_l$	$b_l$
1	$0.2866924170 \times 10^{-1}$	0
2	$-0.3554066483 \times 10^2$	-5/4
3	$-0.8003312290 \times 10^2$	-3/2
4	$-0.1388893486 \times 10^{11}$	-11/2
5	$0.3663978029 \times 10^{11}$	-23/4
$l$	$C_l$	$c_l$
1	$0.2850918168 \times 10^6$	-11/4
2	$-0.1472740048 \times 10^9$	-7/2
3	$0.6616737314 \times 10^9$	-15/4
4	$-0.1262999051 \times 10^{11}$	-9/2
5	$0.3794222032 \times 10^{12}$	-21/4
6	$-0.6465333262 \times 10^{12}$	-11/2

$$z(\rho, T) = 1 + B(T) \left( \frac{\rho}{M} \right) + C(T) \left( \frac{\rho}{M} \right)^2 + \dots, \quad (\text{A5})$$

which we truncate after the third term. In this equation,  $M$  is the molar mass and  $B$  and  $C$  are the second and third virial coefficient, respectively, which are modeled by using the equations provided by Stewart and Jacobsen<sup>35</sup> (Table III)

$$B(T) = \sum_{i=1}^5 B_i T^{b_i}, \quad C(T) = \sum_{i=1}^6 C_i T^{c_i}, \quad (\text{A6})$$

with these expression we write Eqs. (12), (13), and (17) as

$$K \frac{D}{Dt} \begin{pmatrix} \rho \\ u \\ T \end{pmatrix} = \begin{pmatrix} -\frac{1}{A} \frac{DA}{Dt} \\ \frac{\rho^2}{1-g} \beta_\rho \frac{Dg}{Dt} \\ (RT-L) \frac{Dg}{Dt} \end{pmatrix}, \quad (\text{A7})$$

where  $K$  is a matrix

$$K = \begin{pmatrix} \frac{1}{\rho} & \frac{1}{u} & 0 \\ \beta_\rho & u & \beta_T \\ \frac{p}{\rho^2} & 0 & -(c_v + gR) \end{pmatrix}. \quad (\text{A8})$$

The system Eq. (A7) can be solved for  $\rho$ ,  $u$ , and  $T$  when the right hand side is given. The term  $-\frac{1}{A} \frac{DA}{Dt}$  is determined by the nozzle geometry so we are left with  $\frac{Dg}{Dt}$  which is obtained by differentiating Eq. (21)

$$\frac{Dg}{Dt} = \frac{D}{Dt} \left( \frac{4}{3} \pi \rho_L \hat{\mu}_3 \right) \approx \frac{4}{3} \pi \rho_L \frac{D\hat{\mu}_3}{Dt}. \quad (\text{A9})$$

The moment transport equation (23), the system equation (A7), and finally Eq. (A9) form a closed set of differential equations that can be solved in the diverging supersonic part of the nozzle in a downstream space-marching manner. The

required throat conditions are obtained by integrating the energy equation (14) and the entropy equation (17) from reservoir conditions to sonic conditions.

- <sup>1</sup>V. P. Krainov and M. B. Smirnov, *Phys. Rep.* **370**, 237 (2002).
- <sup>2</sup>T. Nagashima, H. Hirayama, K. Shibuya, M. Hangyo, M. Hashida, S. Tokita, and S. Sakabe, *Opt. Express* **17**, 8907–8912 (2009).
- <sup>3</sup>T. D. Donnelly, T. Ditmire, K. Neuman, M. D. Perry, and R. W. Falcone, *Phys. Rev. Lett.* **76**, 2472 (1996).
- <sup>4</sup>C. Vozzi, M. Nisoli, J-P. Caumes, G. Sansone, S. Stagira, S. De Silvestri, M. Vecchiocattivi, D. Bassi, M. Pascolini, L. Poletto, P. Villorosi, and G. Tondello, *Appl. Phys. Lett.* **86**, 111121 (2005).
- <sup>5</sup>A. G. York, H. M. Milchberg, J. P. Palastro, and T. M. Antonsen, *Phys. Rev. Lett.* **100**, 195001 (2008).
- <sup>6</sup>T. Ditmire, J. Zweiback, V. P. Yanovsky, T. E. Cowan, G. Hays, and K. B. Wharton, *Nature* **398**, 489–492 (1999).
- <sup>7</sup>B. D. Layer, A. York, T. M. Antonsen, S. Varma, Y.-H. Chen, Y. Leng, and H. M. Milchberg, *Phys. Rev. Lett.* **99**, 035001 (2007).
- <sup>8</sup>E. A. Gibson, A. Paul, N. Wagner, R. Tobey, D. Gaudiosi, S. Backus, I. P. Christov, A. Aquila, E. M. Gullikson, D. T. Attwood, M. M. Murnane, and H. C. Kapteyn, *Science* **302**, 95–98 (2003).
- <sup>9</sup>H. Ruf, C. Handschin, R. Cireasa, N. Thire, A. Ferre, S. Petit, D. Descamps, E. Mevel, E. Constant, V. Blanchet, B. Fabre, and Y. Mairesse, *Phys. Rev. Lett.* **110**, 083902 (2013).
- <sup>10</sup>S. J. Yoon, A. J. Goers, G. A. Hine, J. D. Magill, J. A. Elle, Y.-H. Chen, and H. M. Milchberg, *Opt. Express* **21**, 15878 (2013).
- <sup>11</sup>K. A. Strelitzky, Y. Zvinevich, B. E. Wyslouzil, and R. Strey, *J. Chem. Phys.* **116**, p. 4058 (2002).
- <sup>12</sup>S. Sinha, H. Laksmono, and B. E. Wyslouzil, *Rev. Sci. Instrum.* **79**, 114101 (2008).
- <sup>13</sup>O. F. Hagen, *Surf. Sci.* **106**, 101 (1981).
- <sup>14</sup>L. Huang and J. B. Young, *Proc. R. Soc. London A* **452**, 1459 (1996).
- <sup>15</sup>O. F. Hagen, *Rev. Sci. Instrum.* **63**, 2374 (1992).
- <sup>16</sup>K. Y. Kim, V. Kumarappan, and H. M. Milchberg, *Appl. Phys. Lett.* **83**, 3210–3212 (2003).
- <sup>17</sup>K. C. Gupta, N. Jha, P. Deb, D. R. Mishra, and J. K. Fuloria, *J. Appl. Phys.* **118**, 114308 (2015).
- <sup>18</sup>S. Jinno, Y. Fukuda, H. Sakaki, A. Yogo, M. Kanasaki, K. Kondo, A. Ya. Faenov, I. Yu. Skobelev, T. A. Pikuz, A. S. Boldarev, and V. A. Gasilov, *App. Phys. Lett.* **102**, 164103 (2013).
- <sup>19</sup>D. G. Jang, Y. S. You, H. M. Milchberg, H. Suk, and K. Y. Kim, *App. Phys. Lett.* **105**, 021906 (2014).
- <sup>20</sup>X. Gao, A. V. Arefiev, R. C. Korzekwa, X. Wang, B. Shim, and M. C. Downer, *J. Appl. Phys.* **114**, 034903 (2013).
- <sup>21</sup>X. Gao, R. Korzekwa, X. Wang, B. Shim, A. V. Arefiev, and M. C. Downer, Conference on Lasers and Electro-Optics, CLEO, 6327169 (2012).
- <sup>22</sup>F. Dorchies, F. Blasco, T. Caillaud, J. Stevefelt, C. Stenz, A. S. Boldarev, and V. A. Gasilov, *Phys. Rev. A* **68**, 023201 (2003).
- <sup>23</sup>A. S. Boldarev, V. A. Gasilov, A. Y. Faenov, Y. Fukuda, and K. Yamakawa, *Rev. Sci. Instrum.* **77**, 083112–083110 (2006).
- <sup>24</sup>F. B. Sprow and J. M. Prausnitz, *Trans. Faraday Soc.* **62**, 1097–1104 (1966).
- <sup>25</sup>Ch. Tegeler, R. Span, and W. Wagner, *J. Phys. Chem. Ref. Data* **28**, 779 (1999).
- <sup>26</sup>M. Hipp, J. Woisetschlager, P. Reiterer, and T. Neger, *Measurement* **36**, 53–66 (2004).
- <sup>27</sup>G. Chen, B. Kim, B. Ahn, and D. E. Kim, *J. Appl. Phys.* **5**, 053507 (2009).
- <sup>28</sup>P. G. Hill, *J. Fluid Mech.* **25**, 593 (1966).
- <sup>29</sup>R. Hagmeijer, *Phys. Fluids* **16**, 176–183 (2006).
- <sup>30</sup>R. Hagmeijer, R. H. A. IJzermans, and F. Put, *Phys. Fluids* **17**, 056101 (2005).
- <sup>31</sup>V. I. Kalikmanov, *Nucleation Theory* (Springer, Dordrecht, 2013), ISBN 9789048136421.
- <sup>32</sup>D. Kashchiev, *Nucleation* (Butterworth-Heinemann, Oxford, 2000), ISBN 9780750646826.
- <sup>33</sup>R. S. R. Sidin, R. Hagmeijer, and U. Sachs, *Phys. Fluids* **21**, 073303 (2009).
- <sup>34</sup>R. C. Reid, J. M. Prausnitz, and B. E. Poling, *The Properties of Gases and Liquids* (McGraw-Hill International Editions, Singapore, 1988), ISBN0-07-100284-7.
- <sup>35</sup>R. B. Stewart and R. T. Jacobsen, *J. Phys. Chem. Ref. Data* **18**, 639 (1989).